

# STONet: A novel neural operator for modeling solute transport in micro-cracked reservoirs

Ehsan Haghighat<sup>1,\*</sup>, Mohammad Hesani Adeli<sup>2</sup>, S. Mohammad Mousavi<sup>3</sup>,  
and Ruben Juanes<sup>1</sup>

<sup>1</sup>Massachusetts Institute of Technology, Cambridge, MA

<sup>2</sup>Sharif University of Technology, Tehran, Iran

<sup>3</sup>Cornell University, Ithaca, NY

\*Corresponding author: [ehsanh@mit.edu](mailto:ehsanh@mit.edu)

## Abstract

In this work, we develop a novel neural operator, the Solute Transport Operator Network (STONet), to efficiently model contaminant transport in micro-cracked reservoirs. The model combines different networks to encode heterogeneous properties effectively. By predicting the concentration rate, we are able to accurately model the transport process. Numerical experiments demonstrate that our neural operator approach achieves accuracy comparable to that of the finite element method. The previously introduced Enriched DeepONet architecture has been revised, motivated by the architecture of the popular multi-head attention of transformers, to improve its performance without increasing the compute cost. The computational efficiency of the proposed model enables rapid and accurate predictions of solute transport, facilitating the optimization of reservoir management strategies and the assessment of environmental impacts. The data and code for the paper will be published at <https://github.com/ehsanhaghighat/STONet>.

**Keywords:** Neural Operators; Porous Media; Solute Transport.

## 1. Introduction

The depletion of freshwater resources is a pressing global challenge, particularly in regions facing severe droughts leading to the rapid exhaustion of groundwater reserves. A significant factor contributing to water quality degradation in underground aquifers is the intrusion of seawater: the higher density of saline water facilitates its rapid dispersion and mixing within freshwater aquifers, leading to the groundwater contamination [5, 6]. Assessing the risk of seawater intrusion and developing mitigating strategies requires quantitative modeling of coupled flow and solute transport in porous media [1, 28].

These assessments are further complicated by the common occurrence of fractures in the subsurface, which can significantly alter the flow: typically, fractures exhibit higher permeability than the surrounding domain, thus profoundly modulating groundwater flow and transport [12, 23, 30, 7, 8, 16].

Accounting for fractures in the modeling process generally increases the complexity of the computational models of groundwater flow and transport [7, 17]. However, in cases where the size of fractures is much smaller than other dimensions of interest, upscaling approaches like the equivalent continuum model can be employed to implicitly incorporate the impact of these so-called micro-fractures in the modeling framework [26, 36, 14]. Khoei et al. [15] employed this approach extensively in their study by introducing inhomogeneities in the form of micro- and macro-fractures into a homogeneous benchmark problem known as Schincariol [29, 24]. Their investigation focused on assessing the influence of micro-fractures, both in the presence and absence of macro-fractures, on solute transport in the medium. This study leverages their work to create a dataset for training a neural operator.

**Machine learning (ML)** Over the past few years, there has been an explosive increase in the development and application of deep learning (DL) approaches, partly as a result of data availability and computing power [20]. Recent advances in deep learning approaches have pushed engineers and scientists to leverage ML frameworks for solving classical engineering problems. A recent class of DL methods, namely, Physics-Informed Neural Networks (PINNs), have received increased attention for solving forward and inverse problems and for building surrogate models with lesser data requirements [27, 13, 4]. PINNs leverage physical principles and incorporate them into the optimization process, enabling the network to learn the underlying physics of the problem. The applications of this approach extend to fluid mechanics, solid mechanics, heat transfer, and flow in porous media, among others [9, 3, 25, 10, 2, 11]. A recent architecture, namely Neural Operators, provides an efficient framework for data-driven and physics-informed surrogate modeling [22, 21, 33, 34, 19]. Neural Operators are a class of neural networks that operate on functions rather than vectors, enabling them to capture the relationships between input and output functions. By leveraging the power of Neural Operators, it is possible to construct surrogate models that are both data-efficient and accurate. This makes Neural Operators well-suited for problems where experimental data is limited or computationally expensive to obtain. Once trained, neural operators can be used to perform inference efficiently.

**Our contributions** In this study, we developed a novel neural operator specifically designed for modeling density-driven flow in fractured porous media. The neural operator leverages the power of deep learning to capture the complex relationships between the equivalent permeability tensor, which is a result of variations in fracture orientation and fracture density, and the pressure gradient, and output the temporally varying concentration field. The new architecture, as detailed in section 3.2, revises the previously

introduced En-DeepONet [11] to achieve higher accuracy at the same computational cost. 71

We generated a comprehensive dataset obtained using high-fidelity finite element sim- 72  
ulations to train and validate the neural operator. This dataset serves as a reliable 73  
benchmark for evaluating the performance of the proposed neural operator. We applied 74  
the developed framework to predict flow patterns in porous media under heterogeneous 75  
conditions, demonstrating its ability to handle complex geological scenarios. 76

## 2. Governing Equations 77

The governing equations describing the solute transport in fractured porous media include 78  
the mass conservation equation for the fluid phase and solute component. The fluid mass 79  
conservation is expressed as 80

$$\frac{\partial}{\partial t}(\phi\rho) + \nabla \cdot (\rho\mathbf{v}_m) = 0, \quad (1)$$

where  $\phi$  represents the matrix porosity,  $\rho$  denotes the fluid density that varies with the 81  
solute mass fraction (concentration), and  $\mathbf{v}_m$  is the fluid phase velocity vector within the 82  
matrix. This velocity can be expressed in terms of pressure by applying Darcy's law as 83

$$\mathbf{v}_m = -\frac{\mathbf{k}_m}{\mu} (\nabla p - \rho\mathbf{g}). \quad (2)$$

Here,  $\mu$  denotes the fluid viscosity,  $\mathbf{g}$  represents the gravitational acceleration, and  $\mathbf{k}_m$  84  
stands for the permeability tensor of the matrix. In eq. (1), it is assumed that the fluid is 85  
incompressible and the matrix porosity remains constant over time. Substituting Darcy's 86  
law into eq. (1) and neglecting density variations except in the terms involving gravity 87  
(Boussinesq approximation [35, 7]), one obtains 88

$$\nabla \cdot \left( -\frac{\mathbf{k}_m}{\mu} (\nabla p - \rho\mathbf{g}) \right) = 0. \quad (3)$$

As stated earlier, the density is a function of the solute mass fraction. Assuming a linear 89  
state equation [6], the density function is expressed as 90

$$\rho(c) = \rho_0 + \frac{\rho_s - \rho_0}{\rho_0} c, \quad (4)$$

where  $c$  is the mass fraction, taking a value between 0 and 1, and  $\rho_0$  and  $\rho_s$  are the 91  
reference values for the fluid density at zero mass fraction (pure water) and at unit mass 92  
fraction (pure solute), respectively. Additionally,  $\mathbf{k}_m$  is influenced by both the intrinsic 93  
permeability of the pore structure and the geometric characteristics of micro-fractures. 94  
To compute  $\mathbf{k}_m$ , the domain must be divided into Representative Elementary Volumes 95  
(REV). For each REV, the specific permeability matrix can be determined using the 96

equivalent continuum model, outlined in [15], as

$$\mathbf{k}_m = \mathbf{k}_r + \frac{1}{12\Sigma} \sum_i b_i^3 l_i \mathbf{M}_i. \quad (5)$$

The first part of the equivalent permeability tensor eq. (5), i.e.,  $\mathbf{k}_r$ , is an isotropic tensor related to the intrinsic permeability of the pore structure. Variables  $b_i$  and  $l_i$  correspond to the aperture and length of micro-fractures, respectively.  $\Sigma$  is the volume of the REV, and  $\mathbf{M}_i$  denotes the conversion matrix defined as

$$\mathbf{M}_i = \mathbf{I} - \mathbf{n}_i \otimes \mathbf{n}_i, \quad (6)$$

where  $\mathbf{n}_i$  is the unit vector normal to the  $i^{\text{th}}$  micro-fracture. Note that, while  $\mathbf{k}_r$  is an isotropic tensor,  $\mathbf{M}_i$  is anisotropic due to the varied orientations of the micro-fractures.

The next governing equation pertains to the conservation of mass for the solute within the fluid phase and can be written as

$$\phi \frac{\partial}{\partial t} (\rho c) + \nabla \cdot (\rho c \mathbf{v}_m) - \nabla \cdot (\rho \mathbf{D}_m \nabla c) = 0, \quad (7)$$

in which Fick's law is used for the dispersive and diffusive flux of solute components.  $\mathbf{D}_m$  is the dispersion-diffusion tensor, which is a function of the velocity  $\mathbf{v}_m$ , and expressed as

$$\mathbf{D}_m = \phi \tau D_m \mathbf{I} + (\alpha_L - \alpha_T) \frac{\mathbf{v}_m \otimes \mathbf{v}_m}{|\mathbf{v}_m|} + \alpha_T |\mathbf{v}_m| \mathbf{I}. \quad (8)$$

Here, the first term in eq. (7) denotes the rate of change in the mass of the solute component, while the second and third terms denote the advective and dispersive transport mechanisms of the solute component, respectively.  $D_m$  refers to the molecular diffusion coefficient associated with the matrix,  $\tau$  represents the tortuosity of the porous medium,  $\mathbf{I}$  is the identity tensor and  $\alpha_L$  and  $\alpha_T$  denotes the longitudinal and transverse dispersivities, respectively. The solution to the aforementioned equations can be achieved through the finite element method, as detailed in [15].

### 3. STONet: Neural Operator for solute transport in fractured porous media

Neural operators are a class of machine learning models designed to learn mappings between infinite-dimensional function spaces. They are particularly well-suited for solving parameterized partial differential equations (PDEs) that arise in various physical phenomena. Unlike traditional neural networks that operate on fixed-dimensional vectors, neural operators can handle functions as inputs and outputs, making them ideal for constructing surrogate models for continuous space-time problems. In this section, we review neural

operators in general and then provide details about the specifics of STONet. 123

### 3.1 Enriched DeepONet 124

The goal of a neural operator is to learn a mapping  $G : U \rightarrow V$  between two function spaces  $U$  and  $V$ . For the problem of solute transport,  $U$  might represent the space of initial and boundary conditions, fracture properties such as orientation, length, and opening, and medium parameters such as permeability and porosity, while  $V$  represents the space of the solute concentration field over time. A neural operator typically consists of two main components: (1) a feature-encoding network, known as the branch network (B); and (2) a query network, known as the trunk network (T). They process the input function  $u \in U$  and encode relevant features. The final output of the neural operator is obtained by combining the outputs of the branch and trunk networks through a suitable operation, such as elementwise multiplication or a learned fusion mechanism (a final network).

DeepONet and its generalization Enriched-DeepONet [11] have proven a good candidate for learning continuous functional spaces. The neural architecture for En-DeepONet is depicted in fig. 1(a), and expressed mathematically as

$$\epsilon_B = B(u; \boldsymbol{\theta}_B), \quad (9)$$

$$\epsilon_T = T(x; \boldsymbol{\theta}_T), \quad (10)$$

$$G(u)(x) = R(\epsilon_{B \odot T}, \epsilon_{B \oplus T}, \epsilon_{B \ominus T}; \boldsymbol{\theta}_R), \quad (11)$$

where  $x \in X$  and  $u \in U$  are a query point in the solution domain  $\Omega$  and a problem parameter set, respectively. Here,  $\boldsymbol{\theta}_\alpha$  represents the set of parameters of each network, and  $\epsilon_B, \epsilon_T$  are encoded outputs of branch and trunk networks, respectively.  $\odot, \oplus, \ominus$  denotes elementwise multiplication, addition, and subtraction of branch and trunk encodings, respectively.  $R$  is a fusion network, known as the root network, which decodes the final outputs.

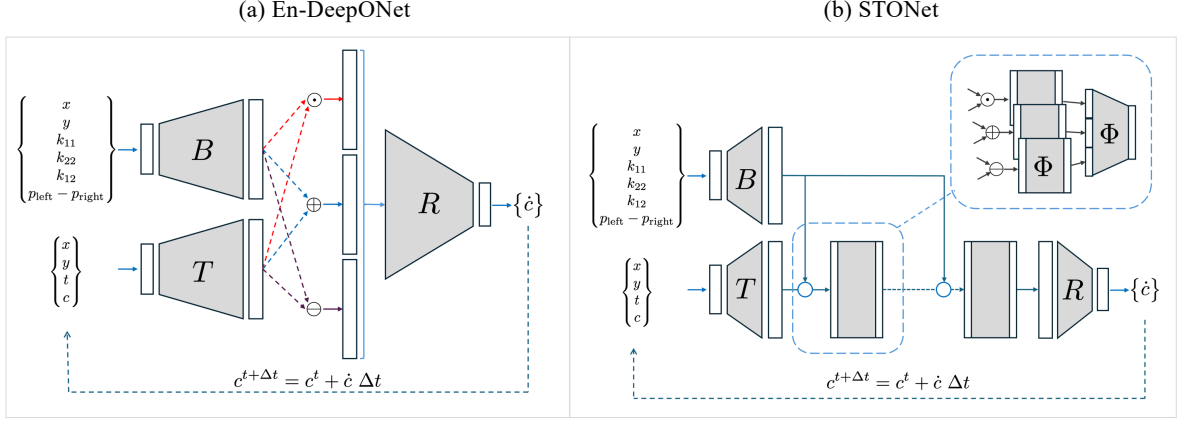


Figure 1: Network architecture. (a) En-DeepONet neural architecture. (b) The revised En-DeepONet architecture, namely STONet. STONet resembles the multi-head attention mechanism of transformer architecture and applies the multiplication, addition, and subtraction operations on different layers.

### 3.2 STONet

144

Here, we present an extension of the En-DeepONet architecture that resembles the multi-  
 head attention mechanism of transformer networks [31]. The network architecture is  
 depicted in fig. 1(b). The architecture consists of an encoding branch and a trunk network.  
 The output of the branch network is then combined with the output of the trunk network,  
 using elementwise operations such as multiplication or addition, and passed to the new  
 attention block. One may add multiple attention blocks. The final output is then passed  
 on to the output root network. The network architecture is expressed mathematically as

145

146

147

148

149

150

151

$$\epsilon_B = B(u; \boldsymbol{\theta}_B), \quad (12)$$

$$\epsilon_T = T(x; \boldsymbol{\theta}_T), \quad (13)$$

$$\epsilon_Z^0 = \epsilon_T, \quad (14)$$

$$\epsilon_{B \odot Z}^l = \Phi(\epsilon_{B \odot Z}^{l-1}; \boldsymbol{\theta}_Z^{\odot, l}), \quad l = 1 \dots L, \quad (15)$$

$$\epsilon_{B \oplus Z}^l = \Phi(\epsilon_{B \oplus Z}^{l-1}; \boldsymbol{\theta}_Z^{\oplus, l}), \quad l = 1 \dots L, \quad (16)$$

$$\epsilon_{B \ominus Z}^l = \Phi(\epsilon_{B \ominus Z}^{l-1}; \boldsymbol{\theta}_Z^{\ominus, l}), \quad l = 1 \dots L, \quad (17)$$

$$\epsilon_Z^l = \Phi(\epsilon_{B \odot Z}^l, \epsilon_{B \oplus Z}^l, \epsilon_{B \ominus Z}^l; \boldsymbol{\theta}_Z^l), \quad l = 1 \dots L, \quad (18)$$

$$G(u)(x) = R(\epsilon_Z^L; \boldsymbol{\theta}_R), \quad (19)$$

where  $\Phi$  denotes a single fully-connected layer, and  $L$  is the total number of attention  
 blocks. Lastly, the network is trained on the concentration rate, therefore concentration  
 field is predicted auto-regressively using the forward Euler update as

152

153

154

$$c^{t+\Delta t} = c^t + G(u)(x) \Delta t. \quad (20)$$

### 3.3 Optimization

155

The optimization of neural operators involves adjusting the parameters of the branch, trunk, and root networks to minimize a loss function that measures the discrepancy between the predicted and true outputs. In this study, the network output is the concentration rate  $\dot{c}$ , as mentioned previously. Hence, the loss function is based on the mean squared error between the predicted and observed solute concentrations. The optimization is performed using the Adam optimizer [18], a variant of the stochastic gradient descent. The gradients are computed using backpropagation through the computational graph of the neural operator. Regularization techniques, such as weight decay or dropout, may be employed to prevent overfitting and improve the generalization of the model.

156  
157  
158  
159  
160  
161  
162  
163  
164

## 4. Results and Discussion

165

In this section, we present the results of our numerical experiments on the performance of the proposed neural operator for surrogate modeling of solute transport in micro-cracked reservoirs. We compare the accuracy and computational efficiency of our approach to the finite element method. Additionally, we evaluate the effectiveness of the neural operator in handling different input scenarios and encoding heterogeneous properties of the porous medium. Finally, we discuss the potential applications of our model in environmental impact assessment and groundwater management.

166  
167  
168  
169  
170  
171  
172

### 4.1 Problem Description

173

A schematic of the problem considered in this study of a solute through a micro-cracked reservoir is shown in fig. 2. The domain under consideration has dimensions of  $70 \times 50$  cm. The solution is injected from the left side and transported through the domain, driven by a pressure difference between the left and right boundaries. The porous reservoir is assumed to be confined between two impervious layers and contains randomly distributed micro-cracks of varying density and orientations. The micro-fracture orientations are sampled randomly from a normal distribution with varying mean values but fixed standard deviation, i.e.,  $\theta \sim \mathcal{N}(\mu_\theta, \sigma_\theta = 15^\circ)$ , where  $\mu_\theta$  is sampled uniformly as  $\mu_\theta \sim \mathcal{U}(-60^\circ, 60^\circ)$ . The representative elementary volume (REV) dimensions for assessing the permeability field (using eq. (5)) are assumed  $10 \times 10$  cm. Fracture density, i.e., the number of cracks per REV, is sampled from a Poisson's distribution as  $\Sigma \sim \mathcal{P}(\lambda)$ , where  $\lambda$  is sampled uniformly as  $\lambda \sim \mathcal{U}(30, 70)$ . Fracture length and aperture are sampled from log-normal distributions  $\log(l_c) \sim \mathcal{N}(\mu_{l_c} = 0.05, \sigma_c = 0.0575)$  and  $\log(a) \sim \mathcal{N}(\mu_a = 1.14 \times 10^{-4}, \sigma_a = 1.15 \times 10^{-4} \times 1.5)$ , respectively. The pressure on the left side is kept fixed, while the pressure on the right side is also randomly perturbed from a normal distribution, i.e.,  $p_{right} = \mathcal{U}(4976, 4996) + 9792.34y$ . fig. 3 depicts a sample medium with micro-fractures.

174  
175  
176  
177  
178  
179  
180  
181  
182  
183  
184  
185  
186  
187  
188  
189

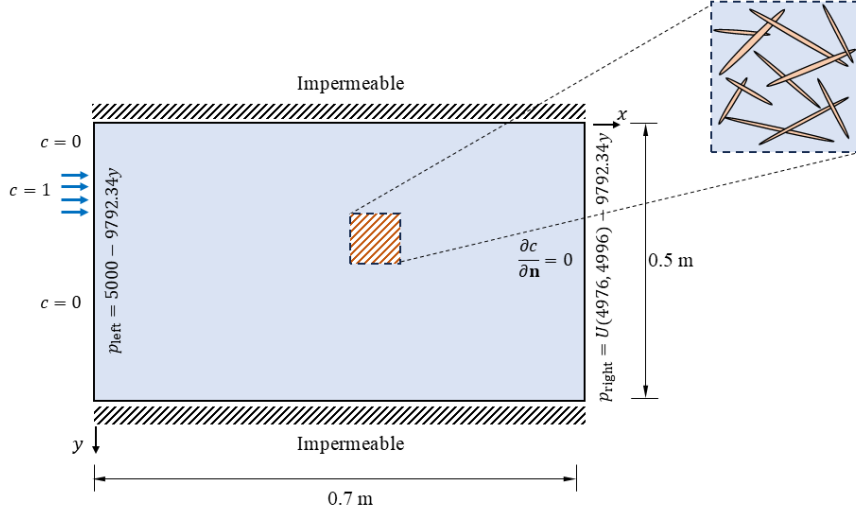


Figure 2: Problem setup. The figure depicts the original problem studied by [29]. The right pressure, as well as microcrack orientation and density (number of fractures per REV), are assigned randomly.

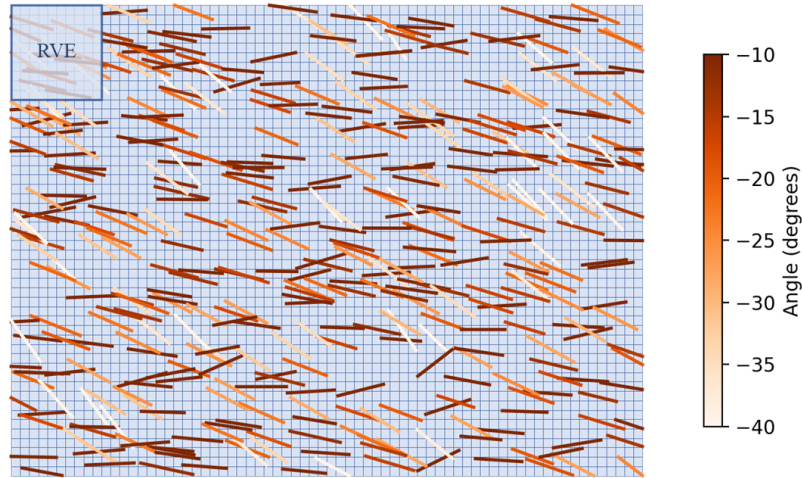


Figure 3: A sample realization of micro-crack distributions.

Figure 4 depicts a few snapshots of the solute concentration for different micro-crack 190  
distributions. The equivalent permeability field  $k_x$  ( $k_{11}$ ) and  $k_y$  ( $k_{22}$ ) are plotted in the left 191  
two columns, while the right two columns highlight concentration and the rate of change 192  
of concentration at the last time step (i.e.,  $t = 36$  hr). The changes in the concentration 193  
patterns are due to different fracture orientations and pressure gradients. 194



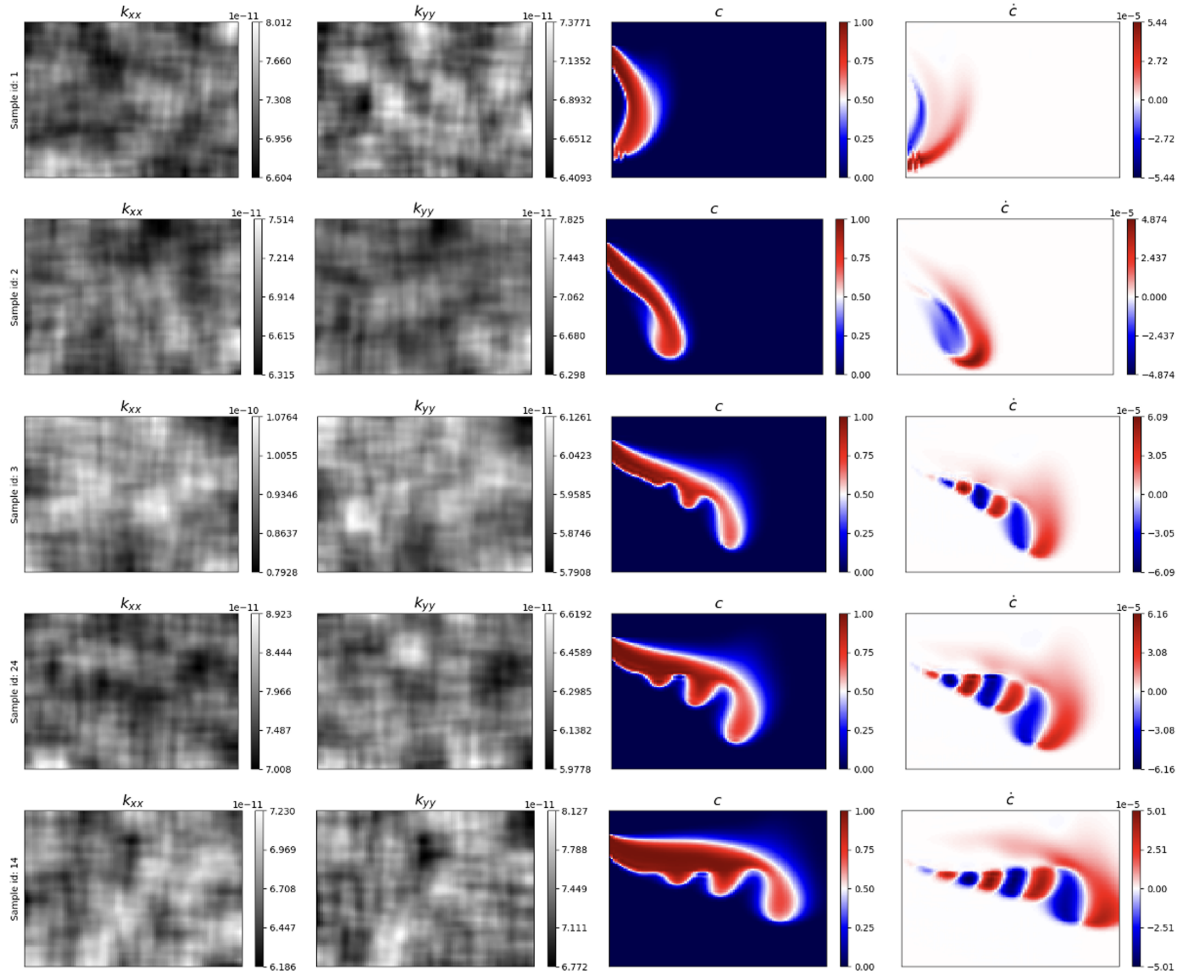


Figure 4: Sample solute concentration for different fracture patterns. Each row represents a different realization of fracture and pressure. The left two columns depict the  $k_{xx}$  and  $k_{yy}$  components of the equivalent permeability tensor. The right two columns represent the concentration and its rate of change, respectively, at the last time step (i.e.,  $t = 36$  h).

The training dataset consists of 500 FEM simulations, and the test dataset consists 195 of 25 random unseen samples. The domain is discretized using an element dimension of 196  $1 \times 1$  cm, resulting in a total of 3,500 elements and 3,621 nodes. We run the simulation for 197 a total of 36 h using 1200 s implicit time increments. However, the outputs are recorded 198 only at 4 h time increments. The generated dataset covers a wide range of fracture 199 densities, orientations, and lengths, providing a diverse set of training examples for our 200 neural operator. 201

## 4.2 Sampling Strategy 202

Since concentration remains near zero for a large portion of the domain (as shown in 203 fig. 4), to reduce the batch size and computational demand, we sub-sample 1,500 random 204 nodes using an importance sampling strategy. Out of these, 1,000 points were selected 205 based on concentration density, while the remaining 500 nodes were uniformly distributed 206 over the domain. 207

### 4.3 Training Performance

208

Let us first compare the performance of the new En-DeepONet architecture (i.e., STONet) 209  
with respect to the original architecture. To this end, we vary the network width and 210  
embedding dimensions in  $\{50, 100\}$ , the number of layers of the branch and trunk networks 211  
in  $\{4, 8, 12\}$ , and the number of the layers of the root network in  $\{4, 8, 12\}$  and number of 212  
attention blocks in  $\{4, 8\}$ . The results are shown in fig. 5, where circles indicate the loss 213  
with the traditional En-DeepONet architecture, and the star symbols the loss with the 214  
new STONet architecture. We observe that for a similar number of parameters, the new 215  
STONet architecture outperforms the previous architecture without an increase in the 216  
computational cost. We also observe that both architectures improve their performance 217  
for larger network widths. 218

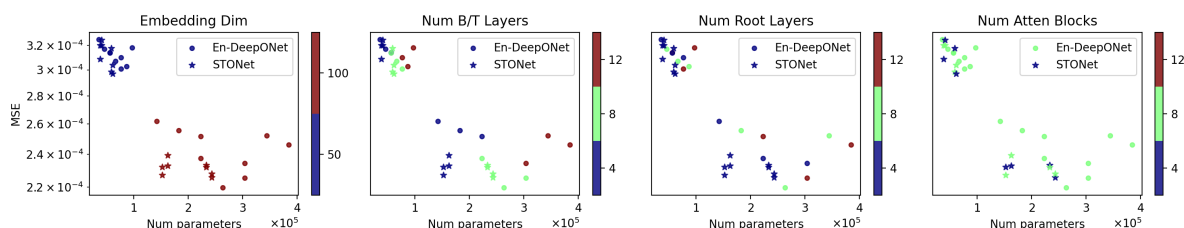


Figure 5: The performance of the new STONet architecture versus the old En-DeepONet architecture. The x-axis shows the total number of parameters, and the y-axis presents the average loss values of the last 20 epochs for training performed for 500 epochs. Each subplot show the variations with respect to the width of the network, number of branch and trunk layers, number of root layers, and number of attention blocks, respectively.

Next, to arrive at the optimal neural architecture for modeling this dataset, we ex- 219  
plored several network sizes. The first variable is the network width of all networks (i.e., 220  
B, T, R,  $\Phi$ ) along with their output dimension (embedding) from  $\{50, 100, 150, 200\}$ . The 221  
second variable is the number of layers in the branch and trunk networks from  $\{2, 4, 8, 12\}$ . 222  
The third variable is the number of attention blocks from  $\{2, 4, 8, 12\}$ . The training is 223  
performed for 2,000 epochs, and the average loss for the last 100 epochs is compared. 224

The results of hyper-parameter exploration are shown in fig. 6. The horizontal axis 225  
shows the total number of parameters, while the vertical axis presents the average of the 226  
loss value for the last 100 epochs. It is apparent that wider networks lead to a significant 227  
improvement in performance. The optimal choice of parameters seems to be 100 for 228  
network width, 8 layers for the branch and trunk networks, 8 attention blocks, and 2 root 229  
layers. Therefore, this architecture is utilized with further training (up to 50,000 epochs) 230  
to arrive at the results presented in the next section. 231

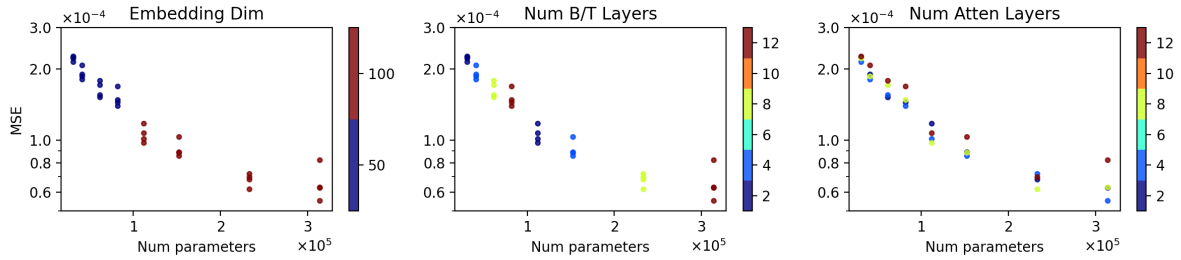


Figure 6: STONet hyper-parameter optimization. The x-axis shows the total number of parameters, and the y-axis presents the average loss values of the last 100 epochs for training performed for 2,000 epochs.

#### 4.4 Model Performance

232

Figure 7 depicts the predictions for the concentration on five random realizations from the test set. The corresponding predictions for the rate of change of concentration are shown in fig. 8. The results from the full-physics simulations for these five test cases were shown earlier in fig. 4. It is apparent that STONet predicts the full-physics results accurately. The fundamental difference is that the STONet, having been pre-trained, can be used for fast prediction of density-driven flow and transport with any new fracture network, while the FEM simulation would need to be recomputed altogether for any new configuration.

233

234

235

236

237

238

239

The distributions for pointwise absolute and relative error at different time steps for concentration and concentration rate are plotted in Figure 9. Overall, STONet's prediction error is very small, with most predictions having below 1% error. The top figures depict the absolute error distributions and highlight the presence of accumulation error as can be observed from widening distributions at different time steps. However, the distribution of relative error at different time steps, as shown in the bottom figures, remains nearly unchanged, indicating a predictable fixed error distribution over time, which is highly desirable. This is also confirmed by inspecting the mean absolute and relative error evolution over time, as plotted in fig. 10. It is worth noting that the accumulation error might be controlled with the addition of observational data and additional training samples using data assimilation techniques such as Active Learning [32].

240

241

242

243

244

245

246

247

248

249

250

## 5. Conclusions

251

In this study, we have presented a new Enriched-DeepONet architecture, STONet, for emulating density-driven flow and solute transport in micro-cracked reservoirs. Our approach effectively encodes heterogeneous properties and predicts the concentration rate, achieving accuracy comparable to that of the finite element method. The computational efficiency of STONet enables rapid and accurate predictions of solute transport, facilitating both parameter identification and groundwater management optimization.

252

253

254

255

256

257

The STONet model developed in this work has the potential to be applied for fracture

258

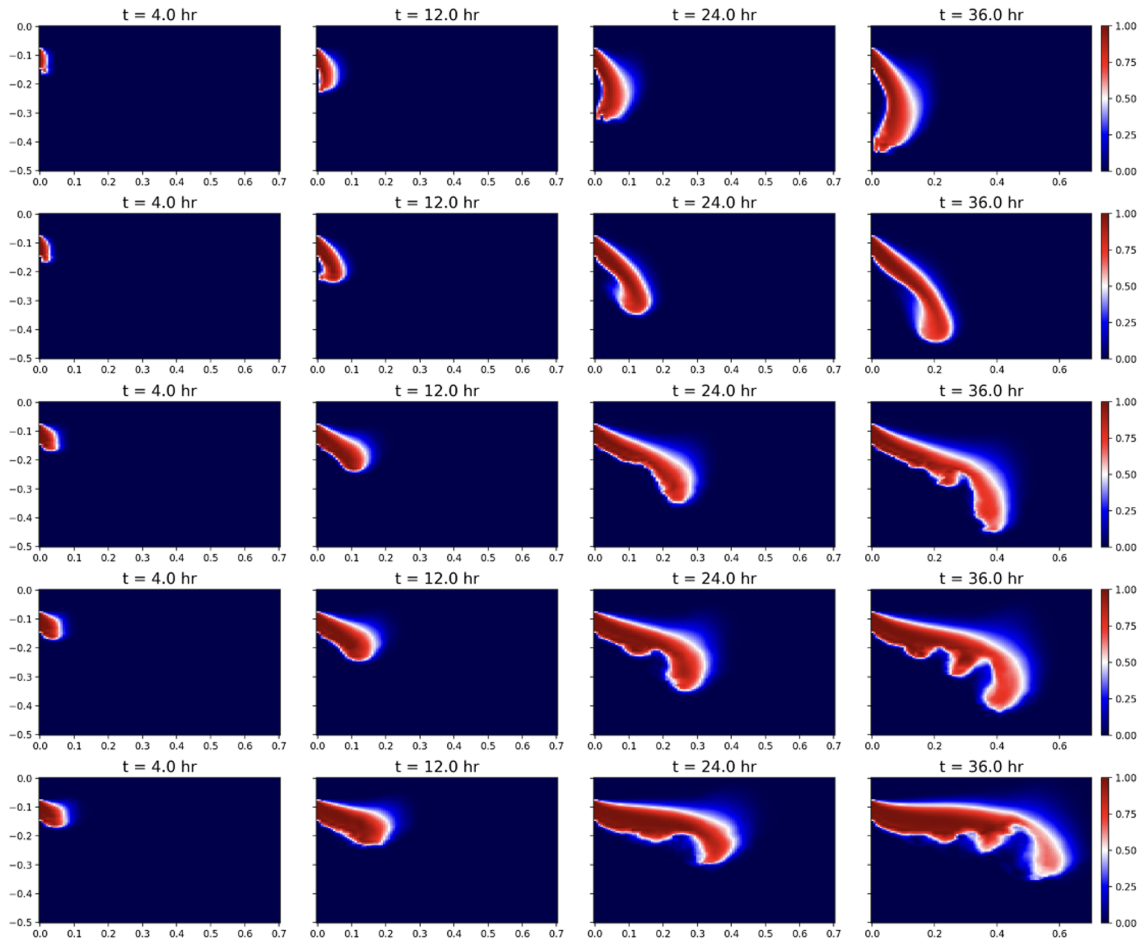


Figure 7: STONet predictions of the concentration field for five samples from the test (unseen) dataset, corresponding to each sample in fig. 7.

network identification and efficient tracing and control of solute transport in micro-cracked reservoirs. By rapidly and accurately predicting the concentration rate, the model can help identify the location and connectivity of fractures in the porous media, which is crucial for optimizing the management of groundwater resources. Additionally, the model can be used to predict the transport of solutes in different scenarios, such as accidental contaminant spills, allowing for accurate and efficient decision-making. Overall, the ML model has the potential to significantly improve the sustainable management of underground aquifers, contributing to both local and global efforts towards sustainable groundwater resource utilization.

## Conflicts of Interest

The authors have no conflicts of interest to declare.

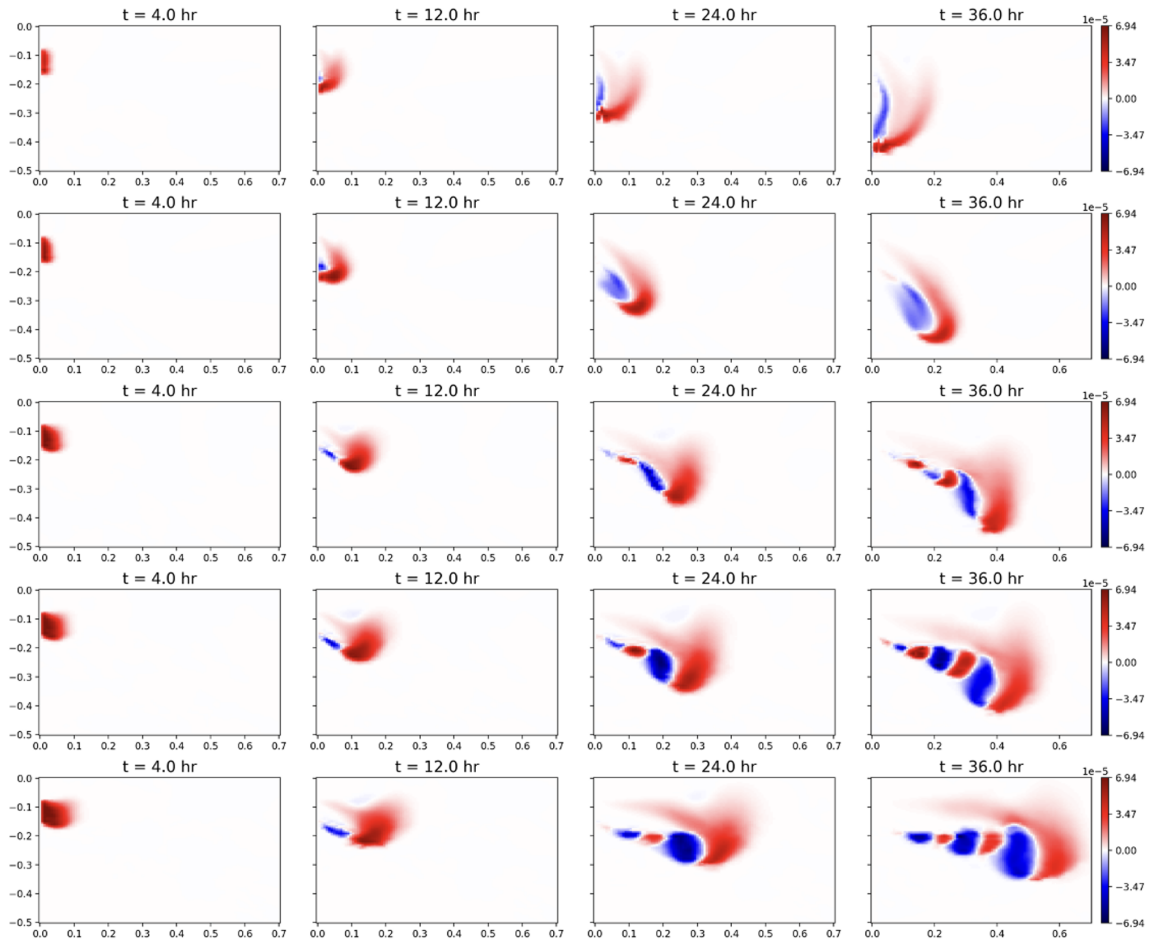


Figure 8: STONet predictions of the rate of change of concentration for five samples from the test (unseen) dataset, corresponding to each sample in fig. 7.

## Author Contributions

270

EH conceptualized the problem and contributed to the theoretical development and im- 271  
 plementation. MHA contributed to the implementation, running the test cases and gener- 272  
 ating the figures. MM prepared the training dataset. All authors contributed to drafting 273  
 and revising the manuscript. 274

## Data availability

275

The data and code for reproducing the results reported in this manuscript will be published 276  
 at <https://github.com/ehsanhaghighat/STONet>. 277

## References

278

- [1] E. Abarca, E. Vázquez-Suñé, J. Carrera, B. Capino, D. Gámez, and F. Batlle. Op- 279  
 timal design of measures to correct seawater intrusion. *Water Resources Research*, 280  
 42(9):W09415, 2006. 281

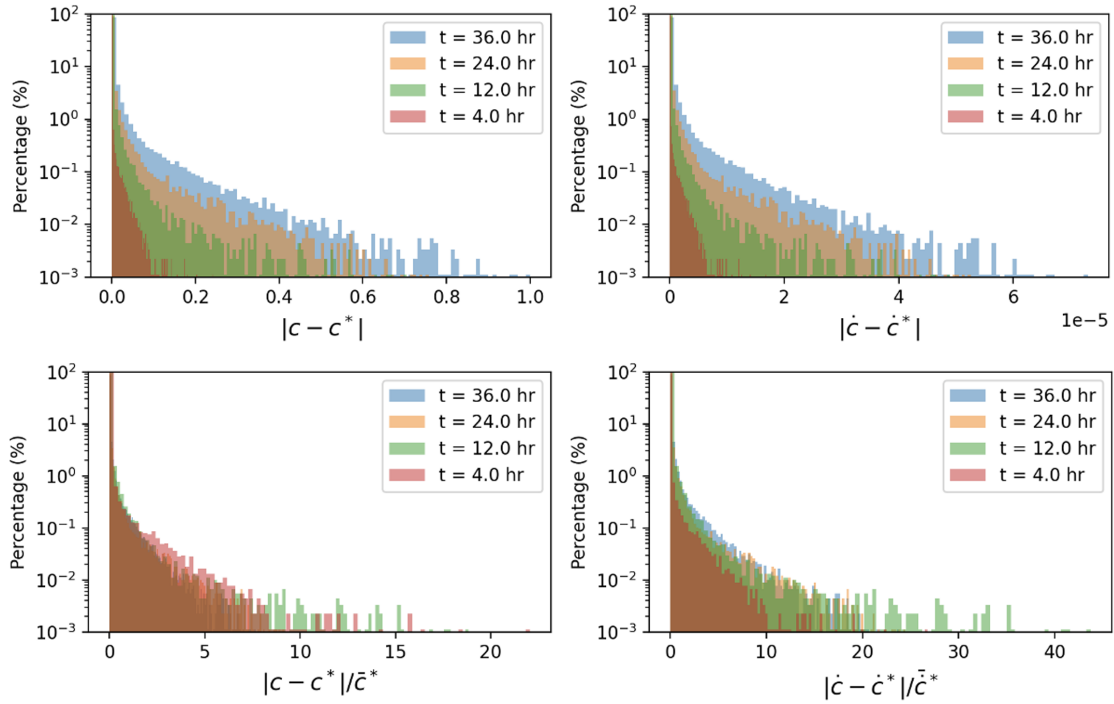


Figure 9: Unrolling error distribution. Pointwise absolute (top row) and relative (bottom row) error distribution for STONet predictions on all 25 test samples at different time steps for (Left) concentration and (Right) concentration rate. The error in the majority of points remains within 1%. While widening absolute error distributions point to error accumulation, the distribution of relative errors remains nearly constant, which is desirable.

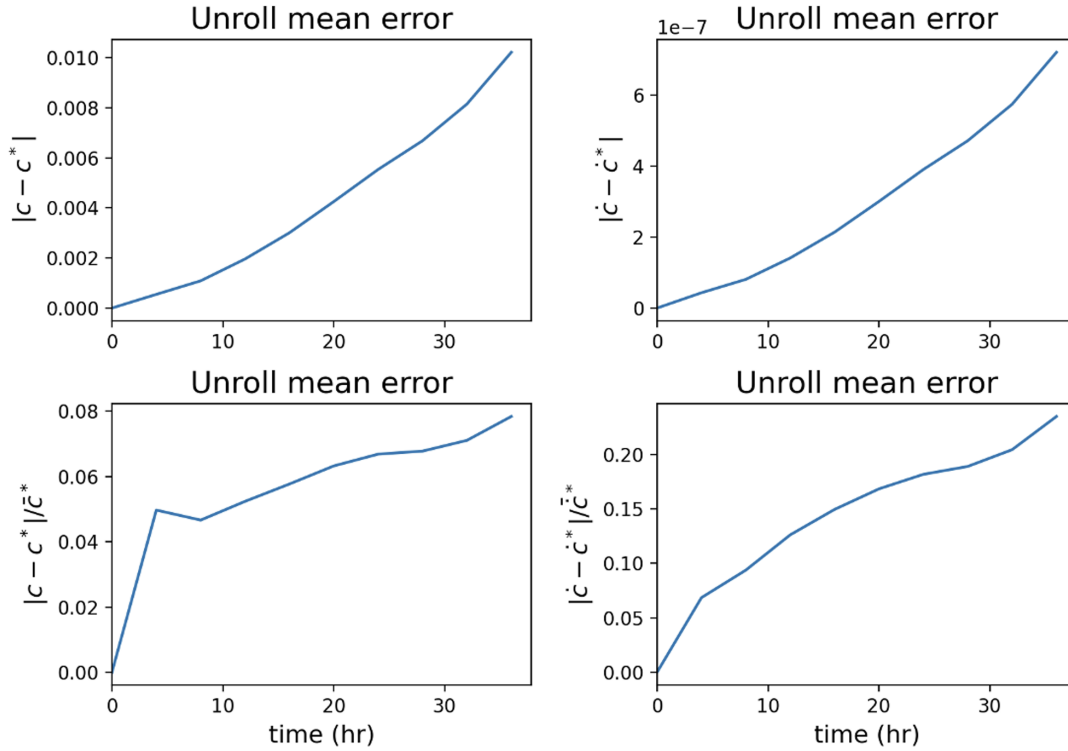


Figure 10: Unrolling error. The plot shows the mean absolute (top row) and relative (bottom row) error of the unrolling process as a result of the auto-regressive nature of the architecture. While the evolution of mean absolute error points to error accumulation, the evolution of mean relative errors remains nearly constant, which is desirable.

- [2] D. Amini, E. Haghghat, and R. Juanes. Physics-informed neural network solution of thermo-hydro-mechanical processes in porous media. *Journal of Engineering Mechanics*, 148(11):04022070, 2022. 282 283 284
- [3] S. Cai, Z. Mao, Z. Wang, M. Yin, and G. E. Karniadakis. Physics-informed neural networks (pinns) for fluid mechanics: A review. *Acta Mechanica Sinica*, 37(12):1727–1738, 2021. 285 286 287
- [4] S. Cuomo, V. S. Di Cola, F. Giampaolo, G. Rozza, M. Raissi, and F. Piccialli. Scientific machine learning through physics-informed neural networks: Where we are and what’s next. *Journal of Scientific Computing*, 92(3):88, 2022. 288 289 290
- [5] M. Dentz, D. Tartakovsky, E. Abarca, A. Guadagnini, X. Sanchez-Vila, and J. Carrera. Variable-density flow in porous media. *Journal of fluid mechanics*, 561:209–235, 2006. 291 292 293
- [6] H.-J. Diersch and O. Kolditz. Variable-density flow and transport in porous media: approaches and challenges. *Advances in water resources*, 25(8-12):899–944, 2002. 294 295
- [7] H.-J. G. Diersch. *FEFLOW: finite element modeling of flow, mass and heat transport in porous and fractured media*. Springer Science & Business Media, 2013. 296 297

- [8] D. Faulkner, C. Jackson, R. Lunn, R. Schlische, Z. Shipton, C. Wibberley, and M. Withjack. A review of recent developments concerning the structure, mechanics and fluid flow properties of fault zones. *Journal of Structural Geology*, 32(11):1557–1575, 2010.
- [9] E. Haghghat, M. Raissi, A. Moure, H. Gomez, and R. Juanes. A physics-informed deep learning framework for inversion and surrogate modeling in solid mechanics. *Computer Methods in Applied Mechanics and Engineering*, 379:113741, 2021.
- [10] E. Haghghat, D. Amini, and R. Juanes. Physics-informed neural network simulation of multiphase poroelasticity using stress-split sequential training. *Computer Methods in Applied Mechanics and Engineering*, 397:115141, 2022.
- [11] E. Haghghat, U. bin Waheed, and G. Karniadakis. En-deeponet: An enrichment approach for enhancing the expressivity of neural operators with applications to seismology. *Computer Methods in Applied Mechanics and Engineering*, 420:116681, 2024.
- [12] R. Juanes, J. Samper, and J. Molinero. A general and efficient formulation of fractures and boundary conditions in the finite element method. *International Journal for Numerical Methods in Engineering*, 54(12):1751–1774, 2002.
- [13] G. E. Karniadakis, I. G. Kevrekidis, L. Lu, P. Perdikaris, S. Wang, and L. Yang. Physics-informed machine learning. *Nature Reviews Physics*, 3(6):422–440, 2021.
- [14] A. Khoei, N. Hosseini, and T. Mohammadnejad. Numerical modeling of two-phase fluid flow in deformable fractured porous media using the extended finite element method and an equivalent continuum model. *Advances in water resources*, 94:510–528, 2016.
- [15] A. Khoei, S. Mousavi, and N. Hosseini. Modeling density-driven flow and solute transport in heterogeneous reservoirs with micro/macro fractures. *Advances in Water Resources*, 182:104571, 2023.
- [16] A. Khoei, S. Saeedmonir, N. Hosseini, and S. Mousavi. An x-fem technique for numerical simulation of variable-density flow in fractured porous media. *MethodsX*, 10:102137, 2023.
- [17] A. R. Khoei and M. Taghvaei. A computational dual-porosity approach for the coupled hydro-mechanical analysis of fractured porous media. *International Journal for Numerical and Analytical Methods in Geomechanics*, 2024.
- [18] D. P. Kingma. Adam: A method for stochastic optimization. *arXiv preprint arXiv:1412.6980*, 2014.



- [19] N. Kovachki, Z. Li, B. Liu, K. Azizzadenesheli, K. Bhattacharya, A. Stuart, and A. Anandkumar. Neural operator: Learning maps between function spaces with applications to pdes. *Journal of Machine Learning Research*, 24(89):1–97, 2023.
- [20] Y. LeCun, Y. Bengio, and G. Hinton. Deep learning. *nature*, 521(7553):436–444, 2015.
- [21] Z. Li, N. Kovachki, K. Azizzadenesheli, B. Liu, K. Bhattacharya, A. Stuart, and A. Anandkumar. Neural operator: Graph kernel network for partial differential equations. *arXiv preprint arXiv:2003.03485*, 2020.
- [22] L. Lu, P. Jin, G. Pang, Z. Zhang, and G. E. Karniadakis. Learning nonlinear operators via deepnet based on the universal approximation theorem of operators. *Nature machine intelligence*, 3(3):218–229, 2021.
- [23] J. Molinero, J. Samper, and R. Juanes. Numerical modeling of the transient hydrogeological response produced by tunnel construction in fractured bedrocks. *Engineering Geology*, 64(4):369–386, 2002.
- [24] J. L. Musuuzza, S. Attinger, and F. A. Radu. An extended stability criterion for density-driven flows in homogeneous porous media. *Advances in water resources*, 32(6):796–808, 2009.
- [25] S. A. Niaki, E. Haghghat, T. Campbell, A. Poursartip, and R. Vaziri. Physics-informed neural network for modelling the thermochemical curing process of composite-tool systems during manufacture. *Computer Methods in Applied Mechanics and Engineering*, 384:113959, 2021.
- [26] M. Oda. An equivalent continuum model for coupled stress and fluid flow analysis in jointed rock masses. *Water resources research*, 22(13):1845–1856, 1986.
- [27] M. Raissi, P. Perdikaris, and G. E. Karniadakis. Physics-informed neural networks: A deep learning framework for solving forward and inverse problems involving nonlinear partial differential equations. *Journal of Computational physics*, 378:686–707, 2019.
- [28] S. Saeedmonir, M. Adeli, and A. Khoei. A multiscale approach in modeling of chemically reactive porous media. *Computers and Geotechnics*, 165:105818, 2024.
- [29] R. A. Schincariol, F. W. Schwartz, and C. A. Mendoza. Instabilities in variable density flows: Stability and sensitivity analyses for homogeneous and heterogeneous media. *Water resources research*, 33(1):31–41, 1997.
- [30] M. L. Sebben, A. D. Werner, and T. Graf. Seawater intrusion in fractured coastal aquifers: A preliminary numerical investigation using a fractured henry problem. *Advances in water resources*, 85:93–108, 2015.

- [31] A. Vaswani. Attention is all you need. *Advances in Neural Information Processing Systems*, 2017. 366 367
- [32] N. Wang, H. Chang, and D. Zhang. Inverse modeling for subsurface flow based on deep learning surrogates and active learning strategies. *Water Resources Research*, 59(7):e2022WR033644, 2023. 368 369 370
- [33] S. Wang, H. Wang, and P. Perdikaris. Learning the solution operator of parametric partial differential equations with physics-informed deepnets. *Science advances*, 7(40):eabi8605, 2021. 371 372 373
- [34] G. Wen, Z. Li, K. Azizzadenesheli, A. Anandkumar, and S. M. Benson. U-fno—an enhanced fourier neural operator-based deep-learning model for multiphase flow. *Advances in Water Resources*, 163:104180, 2022. 374 375 376
- [35] R. K. Zeytounian. Joseph boussinesq and his approximation: a contemporary view. *Comptes Rendus Mecanique*, 331(8):575–586, 2003. 377 378
- [36] C. B. Zhou, R. S. Sharma, Y. F. Chen, and G. Rong. Flow–stress coupled permeability tensor for fractured rock masses. *International Journal for Numerical and Analytical Methods in Geomechanics*, 32(11):1289–1309, 2008. 379 380 381